

Simulation of the QBO in IAP-AGCM: Analysis of momentum budget IAP-AGCM对QBO模拟的动量收支分析

Zhaoyang Chai^{a,b}, Minghua Zhang^{c,*}, Qingcun Zeng^{a,b}, Jinbo Xie^d, Ting You^{b,e}, He Zhang^{a,b}

^a International Center for Climate and Environment Sciences, Institute of Atmospheric Physics, Chinese Academy of Sciences, Beijing, China

^b College of Earth and Planetary Science, University of Chinese Academy of Sciences, Beijing, China

^c School of Marine and Atmospheric Sciences, State University of New York at Stony Brook, NY, USA

^d State Key Laboratory of Numerical Modeling for Atmospheric Sciences and Geophysical Fluid Dynamics, Institute of Atmospheric Physics, Chinese Academy of Sciences, Beijing, China

^e Center for Monsoon System Research, Institute of Atmospheric Physics, Chinese Academy of Sciences, Beijing, China

ARTICLE INFO

Keywords:

QBO
Gravity waves
Momentum budget
Zonal wind
关键词:
平流层准两年振荡
重力波
动量收支
纬向风

ABSTRACT

The quasi-biennial oscillation (QBO), a dominant mode of the equatorial stratospheric (~100–1 hPa) variability, is known to impact tropospheric circulation in the middle and high latitudes. Yet, its realistic simulation in general circulation models remains a challenge. The authors examine the simulated QBO in the 69-layer version of the Institute of Atmospheric Physics Atmospheric General Circulation Model (IAP-AGCM69) and analyze its momentum budget. The authors find that the QBO is primarily caused by parameterized gravity-wave forcing due to tropospheric convection, but the downward propagation of the momentum source is significantly offset by the upward advection of zonal wind by the equatorial upwelling in the stratosphere. Resolved-scale waves act as a positive contribution to the total zonal wind tendency of the QBO over the equator with comparable magnitude to the gravity-wave forcing in the upper stratosphere. Results provide insights into the mechanism of the QBO and possible causes of differences in models.

摘要

平流层准两年振荡 (QBO) 是赤道平流层 (~100–1 hPa) 变率的主要模式, 可对中高纬地区的环流产生重要影响, 但目前利用通用大气环流模式 (GCM) 对其进行准确模拟仍然是一个挑战。本文利用IAP大气环流模式 (IAP-AGCM) 的中高层大气模式版本 (IAP-AGCM69) 对QBO进行模拟, 并对其动量收支情况进行分析。研究发现, QBO主要是由对流活动引起的重力波强迫 (参数化) 引起的, 但该动量强迫被平流层赤道上升流所引起的平流过程显著削弱。模式可分辨尺度的波动强迫对赤道上空的QBO的总纬向风倾向有正贡献, 在上平流层, 其量值大小与参数化的重力波强迫相当。以上结果提供了对QBO形成机制以及模式模拟差异可能原因的认识。

1. Introduction

The quasi-biennial oscillation (QBO) of the zonal-mean zonal wind is the primary mode of variability of the tropical stratosphere. The oscillation consists of easterly and westerly wind regimes alternating in time and propagating downward from about 1 to 100 hPa, with an average period of 28 months (Naujokat, 1986; Baldwin et al., 2001) and a downward propagating speed of ~1 km/month (Yu et al., 2017). It is well known that the QBO is produced by the interactions between waves and mean flow (e.g., Lindzen and Holton, 1968) and mainly driven by the deposition of momentum in the shear zones, which is carried by vertically propagating tropical eastward and westward propagating waves (e.g., Holton and Lindzen, 1972). The QBO has been shown to

impact the strength of the stratospheric polar vortex (the polar stratospheric variability) by modulating the propagation of larger-scale waves into the polar region, which is well-known as the Holton–Tan mechanism (Holton and Tan, 1980). The QBO also impacts the distribution of stratospheric chemical constituents such as ozone and water vapor (Randel and Wu, 1996). Observational studies have suggested that the QBO can impact the extratropical storm tracks (Wang et al., 2018) and modulate the Madden–Julian Oscillation (Kim et al., 2020). Also, the QBO affects mesospheric variability by selectively filtering waves that propagate upward through the tropical stratosphere (Baldwin et al., 2001).

Although the QBO mechanism has been understood for many years, it remains a challenge to simulate the QBO in general circulation models (GCMs), with only a few GCMs being able to reproduce it. In phase 5

* Corresponding author.

E-mail address: minghua.zhang@stonybrook.edu (M. Zhang).

<https://doi.org/10.1016/j.aosl.2020.100021>

Received 6 May 2020; Revised 12 June 2020; Accepted 28 June 2020

Available online 14 December 2020

1674-2834/© 2020 The Authors. Published by Elsevier B.V. on behalf of Institute of Atmospheric Physics, Chinese Academy of Sciences. This is an open access article under the CC BY-NC-ND license (<http://creativecommons.org/licenses/by-nc-nd/4.0/>)

of the Coupled Model Intercomparison Project, only five models could generate the QBO internally (Schenzinger et al., 2017; Butchart et al., 2018). As the QBO results from the wave-mean flow interactions, the waves—including tropical Kelvin waves, mixed Rossby gravity waves, inertial-gravity waves, and small-scale gravity waves (GWs)—need to be correctly represented to simulate a realistic QBO. However, many GCMs still cannot simulate a realistic spectrum of tropical waves because of their low resolution and their deficiencies in the parameterization of small-scale GW forcing (Ricciardulli and Garcia, 2000; Lott et al., 2014). Studies have suggested that an adequately fine vertical resolution (vertical grid spacing of ~ 500 – 700 m) of the troposphere and lower stratosphere is also necessary to simulate the QBO due to the forcing of some resolved waves with small vertical wavelength and the need to capture the wind shear (Giorgetta et al., 2006; Richter et al., 2014; Geller et al., 2016). Garcia and Richter (2019) showed that both the 70-layer and 110-layer versions of the Whole Atmosphere Community Climate Model (WACCM) can simulate the QBO, but the simulated QBO in the 70-layer model is relatively weak and fails to propagate to below 50 hPa. It has been shown that the period of the simulated QBO relates to both the characteristic vertical wavenumber (Scaife et al., 2000) and the GW source strength (Scaife et al., 2000; Giorgetta et al., 2006).

The purpose of this study is to understand the momentum budget in generating the QBO by using simulations from the Institute of Atmospheric Physics Atmospheric General Circulation Model, version 4.1 (IAP-AGCM 4.1). The dominant zonal momentum sources and sinks are diagnosed to highlight the roles of the Brewer–Dobson circulation, non-linear transport, and resolved-scale waves in addition to parameterized GWs. A companion paper will report sensitivities of the model's QBO to model layers, vertical resolution, model top height, and forcing configuration based on the understanding from the momentum budget analysis. The paper is organized as follows. Section 2 describes the model and its configuration. Section 3 presents the results, including an evaluation of the simulated QBO and analysis of the momentum budget. Section 4 contains a summary and discussion.

2. Model and configuration

2.1. Model description

Full details about the model used here, IAP-AGCM 4.1, are given in Zhang (2009), Sun et al. (2012), and Zhang et al. (2013). Briefly, IAP-AGCM 4.1 uses a horizontal resolution of $\sim 1.4^\circ \times 1.4^\circ$ and 30 vertical layers, with the model top at ~ 2.26 hPa. While the newer version, IAP-AGCM 5.0, uses new physical parameterizations of convection, clouds, and other updates (Zhang et al., 2020), IAP-AGCM 4.1 uses the full physical package from the Community Atmosphere Model, version 5 (CAM5; Neale et al., 2012), with only minor adjustments to certain parameters. The parameterization of GWs specifies three dominant wave sources separately—topography, fronts, and convection—following Richter et al. (2010). The regimes of wave propagation, saturation, breaking, and momentum deposition to the mean flow are based on Lindzen (1987). The orographic GW drag source parameterization follows McFarlane (1987) and non-orographic GW source parameterizations follow Richter et al. (2010) and Beres et al. (2004, 2005) as implemented in the WACCM version of CAM5.2. Convectively generated GWs are parameterized to be launched at the top of the convection whenever the deep convection parameterization (Zhang and McFarlane, 1995) is activated. The amplitude of convective GWs is parameterized to be proportional to the square of the maximum tropospheric heating rate due to convection. In particular, the tunable parameter called the “efficiency factor” in the convective GW parameterization can be interpreted as the fraction of time during which the model grid-box is covered by GWs. Richter et al. (2010, 2014) used a varying efficiency factor from 0.1 to 0.55 for different grid-box sizes of the model, and it is set to 0.5 in this study.

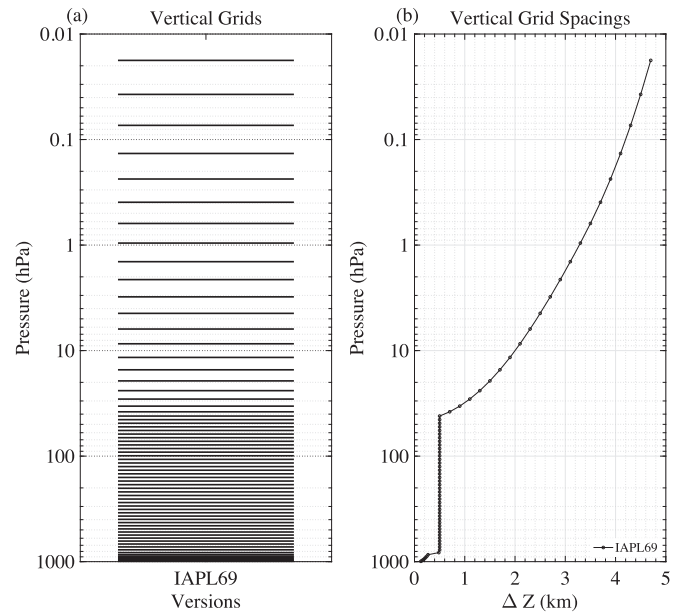


Fig. 1. The (a) vertical grids and (b) vertical grid spacings used in the 69-layer version of IAP-AGCM (IAP-AGCM 4.1). The vertical spacings are about 0.5 km between 800 hPa and 40 hPa, and gradually increase to about 4.6 km near the model top (~ 0.01 hPa).

2.2. Model configuration

In this study, the default 30-layer IAP-AGCM is reconfigured to a 69-layer model—namely, IAP-AGCM4.1 (referred to simply as IAP-AGCM 4.1 hereafter). Fig. 1 shows the vertical grid distribution and its grid spacings for IAP-AGCM 4.1. The vertical resolution is about 0.5 km in the free troposphere and lower stratosphere. The grid spacing then gradually increases to about 4.6 km near the model top at ~ 0.01 hPa. The choices of 69 levels and the model top are somewhat arbitrary but are guided by the model's ability to simulate the QBO. Sensitivities to these choices, including the performance of a 91-layer model (Chai et al., 2020), will be reported in a separate study. The experimental simulation is carried out for the AMIP run type from 1979 to 2005 with prescribed observed global Hadley Centre Sea Surface Temperature and Sea Ice (Taylor et al., 2012).

2.3. Data

All analyses are based on the monthly mean output from IAP-AGCM 4.1 and the monthly mean reanalysis from the ECMWF's third-generation reanalysis product, ERA-Interim (ERA; Dee et al., 2011). The ERA data have 37 pressure levels up to 1 hPa and have a horizontal resolution of $1.5^\circ \times 1.5^\circ$. Zonal wind, meridional wind, temperature, and surface pressure of ERA are used in our analyses.

To eliminate the effects of seasonal variabilities, we removed the annual cycle and its harmonics by subtracting the 27-year (1979–2005; 324 months) average of every month from the dataset to diagnose the QBO signal. Afterwards, we took Fourier analyses on the resulting time series in two ways (Coy et al., 2016) for phase relationships and the amplitudes, respectively. For phase analysis, only one single maximum harmonic signal (period of 27 months for IAP-AGCM 4.1) for a typical QBO was kept via the FFT filter in order to examine the typical phase relations between variables. The energy of the QBO is primarily concentrated around this period, as shown in Fig. S1. For the calculation of amplitudes, a range of periods of 13.5–162 months were kept in order to include the QBO variability. After removing the annual cycle and filtering as described above, the root-mean-square values of the time series were

multiplied by $\sqrt{2}$ as an estimate of the QBO amplitude (Pawson and Fiorino, 1998).

3. Results

3.1. The simulated QBO in the IAPL69

The observed and simulated zonal winds are compared in Fig. 2 by using a 27-year time–pressure cross section of the monthly mean averaged from 2°S to 2°N. Fig. 2(a) shows that in ERAI the typical QBO has an average period of about 28 months. The average of the maximum easterly and westerly is around -40 m s^{-1} and 20 m s^{-1} at $\sim 20 \text{ hPa}$, respectively, implying an asymmetric oscillation of the zonal wind. Fig. 2(b) shows that in IAPL69 the period of the zonal wind oscillation is about 27 months, which is very close to that of ERAI (~ 28 months), but the westerly of the QBO is much stronger ($\sim 35 \text{ m s}^{-1}$ at 7 hPa) than that of ERAI ($\sim 20 \text{ m s}^{-1}$ at 20 hPa), so the easterly is squeezed to a thin band (persisting for ~ 9 months at 7 hPa vs. ~ 16 months at 20 hPa in ERAI) with insufficient downward penetration. This stronger westerly phase also exists in the 60-layer version of CAM5 (Richter et al., 2014), which may be associated with the stronger forcing from the parameterized convectively generated eastward-propagating GWs. The peak value of the amplitude of the simulated oscillation is above 10 hPa , which is mixed with semi-annual oscillation near 1 hPa , while the peak value for ERAI is near $\sim 20 \text{ hPa}$.

The similarities and differences of the simulated QBO amplitude with that in ERAI are more clearly shown in Fig. 3(a, b). The model captures the overall structure of the zonal wind amplitude (Fig. 3(a)), including the poleward extension to $\sim 15^\circ\text{S/N}$, but this extension is a little narrower at lower levels relative to observation, as seen in many GCMs (Schenzinger et al., 2017). The model has a larger amplitude, with a maximum of $\sim 33 \text{ m s}^{-1}$ vs. $\sim 28 \text{ m s}^{-1}$ in ERAI (Fig. 3(b)). In addition, the zonal wind amplitude peaks between ~ 3 and 10 hPa in IAPL69 vs. between ~ 10 and 25 hPa in ERAI. The amplitude distribution of the accompanying temperature in the model is compared with ERAI in Fig. 3(c, d). Consistent with the zonal wind difference, IAPL69 simulates a stronger amplitude in the upper stratosphere and weaker amplitude in the lower stratosphere than ERAI. The maximum amplitude in the model is $\sim 4.6 \text{ K}$ vs. $\sim 3.2 \text{ K}$ in ERAI. Additional experiments indicate drastic sensitivity of these amplitudes to the configuration of model vertical resolution, top height, and the parameterized strength of the wave sources. The higher position of the simulated QBO may be linked with the coarse vertical resolution above 40 hPa in the model, which is too coarse to ac-

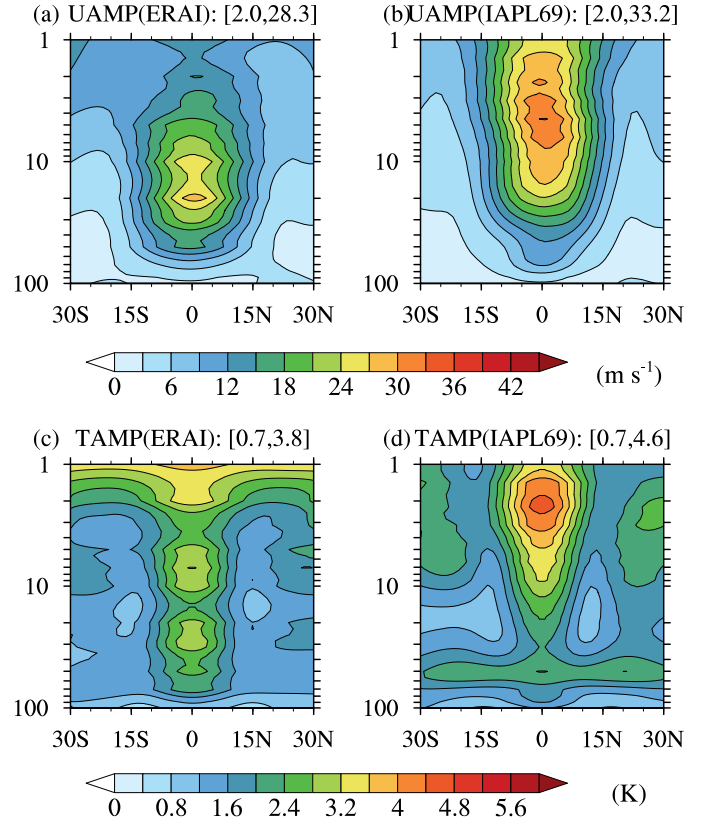


Fig. 3. Amplitudes of de-seasonal (a, b) zonal wind (m s^{-1}) and (c, d) temperature (K) signals of the QBO as a function of latitude and pressure in (a, c) ERAI and (b, d) IAPL69. Maximum and minimum values (rounded) are indicated in the square brackets on the top side of each plot.

curately represent the magnitude of the vertical shear of the zonal wind. Garcia and Richter (2019) showed the difference in the simulated QBO between the 70-layer and 110-layer versions of WACCM. The higher-resolution model better captured the position of the QBO center. This is also consistent in other GCMs (Schenzinger et al., 2017).

3.2. Momentum forcing of the QBO

The zonal momentum equation with a pressure coordinate for IAP-AGCM can be written as

$$\frac{\partial u}{\partial t} = F_D + F_p, \quad (1)$$

where F_D and F_p are u tendencies due to model dynamics and physics, respectively, and t is time. The dynamic term F_D can be written as

$$F_D = -u \frac{\partial u}{\partial x} - v \frac{\partial u}{\partial y} - \omega \frac{\partial u}{\partial p} + f v - \frac{\partial \phi}{\partial x} + F_{hd} + \epsilon. \quad (2)$$

On the right side of Eq. (2), the first three terms are advections, (fv) is the Coriolis effect, $(-\frac{\partial \phi}{\partial x})$ is the pressure gradient term, F_{hd} is horizontal diffusion, and ϵ is u tendency due to numerical effects such as the smoothing filter in IAP-AGCM. Taking the monthly average and then zonal average of Eq. (2), we can obtain the following equation:

$$\begin{aligned} \overline{[F_D]} &= -[\bar{v}] \frac{\partial [\bar{u}]}{\partial y} - [\bar{\omega}] \frac{\partial [\bar{u}]}{\partial p} + f[\bar{v}] + [\bar{F}_{hd}] + [\bar{\epsilon}] \\ &\quad - \frac{\partial}{\partial y} [\bar{v}'u'] - \frac{\partial}{\partial p} [\bar{\omega}'u'] - \frac{\partial}{\partial y} [\bar{v}'u'^*] - \frac{\partial}{\partial p} [\bar{\omega}'u'^*]. \end{aligned} \quad (3)$$

In Eq. (3), $(\bar{\cdot})$ and $[\cdot]$ denote the monthly mean and zonally mean, respectively; $(\cdot)'$ and $(\cdot)^*$ denote the departure from the monthly mean and

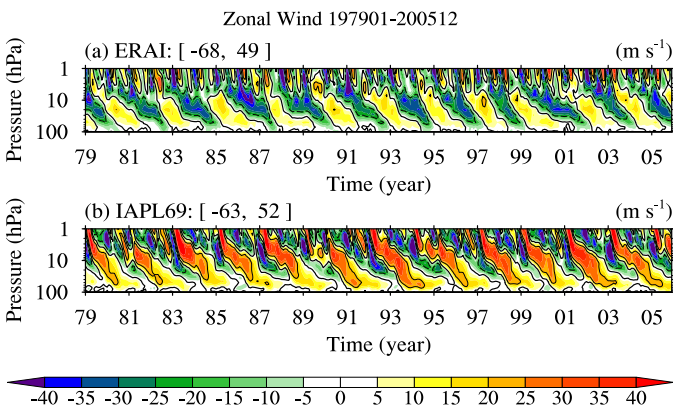


Fig. 2. Time–pressure cross section of the monthly mean zonal wind (filled contours; m s^{-1}) averaged from 2°S to 2°N for the years 1979–2005 for (a) ERAI and (b) IAPL69. Red represents positive (westerly) winds and green negative (easterly). Bold solid, normal solid and dashed black contour lines are 0, 20, and -20 m s^{-1} , respectively. Maximum and minimum values (rounded) of zonal wind are given in the square brackets on the top-left side of each plot.

QBO-filtered Forcing Terms for IAPL69

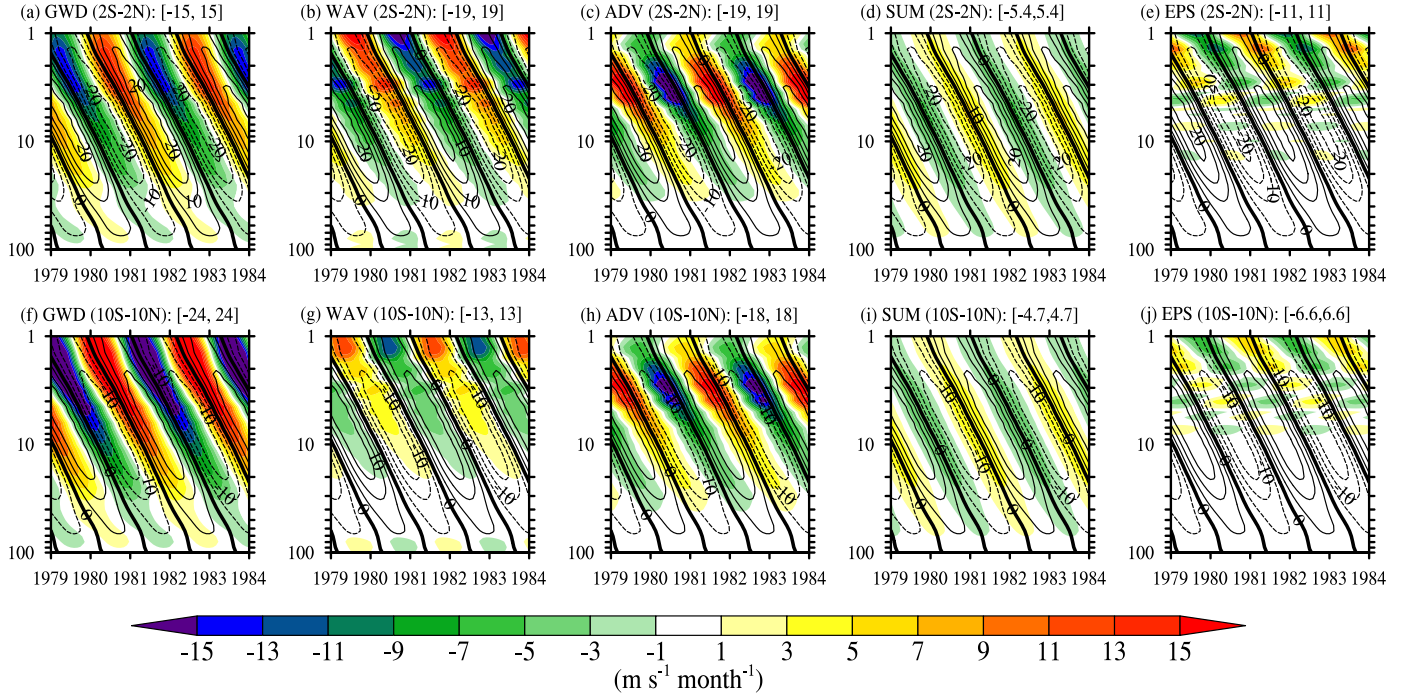


Fig. 4. Time–pressure cross section of simulated QBO-filtered (27-month period) zonal wind tendencies ($\text{m s}^{-1}/\text{month}$; contours shaded red and blue for positive and negative respectively), averaged from 2°S to 2°N in (a–d) and from 10°S to 10°N in (f–i), due to (a, f) GWD (parameterized convective GWs), (b, g) WAV (resolved waves, including vertical and horizontal wave momentum transports), (c, h) ADV (advection, including vertical and horizontal components), and (d, i) SUM (the sum of all the tendencies). Panels (e, j) are the residual terms. The QBO-filtered zonal wind is also plotted (unfilled contour lines; m s^{-1} ; contour interval of 5 m s^{-1} ; solid and dashed lines are positive and negative respectively; zero-lines in heavy bold type). Maximum and minimum values (rounded) of each tendency are given in the square brackets on the top side of each plot.

zonally mean, respectively. The zonal wind tendency due to advection (F_{ADV}) by zonal mean flow is written as

$$F_{\text{ADV}} = -[\bar{v}] \frac{\partial[\bar{u}]}{\partial y} - [\bar{\omega}] \frac{\partial[\bar{u}]}{\partial p}. \quad (4)$$

The zonal wind tendency due to resolved-scale waves (F_{WAV}) is written as

$$F_{\text{WAV}} = -\frac{\partial}{\partial y} [\overline{v'u'}] - \frac{\partial}{\partial p} [\overline{\omega'u'}] - \frac{\partial}{\partial y} [\bar{v}^* \bar{u}^*] - \frac{\partial}{\partial p} [\bar{\omega}^* \bar{u}^*]. \quad (5)$$

On the right side of Eq. (5), the first two terms are associated with transient waves and the last two terms are associated with stationary waves. Actually, the meridional flux ($[\overline{v'u'}]$) for transient waves can be calculated by $[\overline{vu} - \bar{v}\bar{u}]$ (Zhang et al., 2013) where $\bar{v}\bar{u}$ is the monthly-output variable in IAP-AGCM. Also, the vertical flux ($[\overline{\omega'u'}]$) can be calculated by $[\overline{\omega u} - \bar{\omega}\bar{u}]$. As a result, it is the time step of the numerical integration that affects or controls the temporal scale of F_{WAV} . The physics term F_{P} can be decomposed as

$$F_{\text{P}} = F_{\text{dc}} + F_{\text{sc}} + F_{\text{vd}} + F_{\text{rf}} + F_{\text{gw}}, \quad (6)$$

where F_{dc} , F_{sc} , F_{vd} , F_{rf} , and F_{gw} are tendencies due to deep convection (dc), shallow convection (sc), vertical diffusion (vd), Rayleigh Friction (rf), and gravity waves (gw). Here, F_{gw} can be further split into three parts as

$$F_{\text{gw}} = F_{\text{con}} + F_{\text{fro}} + F_{\text{oro}}, \quad (7)$$

where F_{con} , F_{fro} , and F_{oro} are u tendencies due to convective, frontal, and orographic GWs correspondingly.

Based on our diagnosis, we separate the terms on the right-hand side of the zonal wind equation, Eq. (1), into four dominant processes—namely, the GW drag term ($F_{\text{GWD}} = [F_{\text{con}}]$), advection (F_{ADV}), resolved waves (F_{WAV}), and the residual term (F_{RES})—that include all

the terms:

$$\frac{\partial[\bar{u}]}{\partial t} = F_{\text{SUM}} = F_{\text{GWD}} + F_{\text{ADV}} + F_{\text{WAV}} + F_{\text{RES}}. \quad (8)$$

In the following, we show the contribution of these processes to the total zonal wind tendency in generating the QBO.

The forcing from GWD (parameterized convective GWs), ADV (dynamical advection), and WAV (resolved waves) play different roles in the evolution of the QBO. Fig. 4 shows these terms averaged from 2°S to 2°N in the upper row and from 10°S to 10°N in the bottom row. The total tendency (SUM: Fig. 4(d, i)) is plotted over the zonal wind. Since only the peak Fourier component and phase (period of 27 months) are plotted, an identically repeating pattern is formed, which is shown for five years. The SUM tendency peaks in the shear regions as expected, which is relatively homogeneous from 50 to 1 hPa (Fig. 4(d, i)), indicating a phase shift of $\pi/2$ between the SUM tendency (filled contours) and the zonal wind (unfilled contours). It drives the evolution of the QBO wind, forcing downward propagation of the westerly wind and easterly wind alternately. The SUM tendency averaged between 2°S and 2°N is a little larger, with a maximum of $5.4 \text{ m s}^{-1}/\text{month}$ vs. $4.7 \text{ m s}^{-1}/\text{month}$ averaged between 10°S and 10°N .

The GWD tendency (Fig. 4(a, f)) peaks at a phase lag of less than $\pi/4$ behind the SUM tendency and dominates above 10 hPa. The magnitude averaged between 10°S and 10°N (Fig. 4(f)) is much larger, with a maximum of $15 \text{ m s}^{-1}/\text{month}$, than that averaged between 2°S and 2°N , with a maximum of $15 \text{ m s}^{-1}/\text{month}$ (Fig. 4(a)), which may be associated with the meridional double-peak structure of convection in the tropics. The GWD forcing contributes a lot to the SUM tendency and is partly canceled out by other processes.

For the WAV tendency, there are some differences between the 2°S – 2°N average (Fig. 4(b)) and the 10°S – 10°N average (Fig. 4(g)). The former (Fig. 4(b)) peaks at a phase lead of less than $\pi/4$ in advance of the

Table 1 Pearson linear cross-correlations among GWD, WAV, ADV, SUM, and U, averaged for 2°S–2°N and 10°S–10°N, respectively. For example, the figure 0.760 represents the correlation between SUM and WAV of 2°S–2°N; the figure –0.233 represents the correlation between SUM and WAV of 10°S–10°N. The figure in parentheses is the original amplitude of GWD, WAV, ADV, SUM, and U. For GWD, WAV, ADV, and SUM, the unit is $\text{m s}^{-1}/\text{month}$, and for U it is m s^{-1} . The figure in square brackets is the corresponding phase difference, calculated as the inverse cosine of the correlation.

2°S–2°N			10°S–10°N		
Variables	R	$\Delta\phi$	Variables	R	$\Delta\phi$
GWD (10.4) ~U (21.8)	0.462	[0.35 π]	GWD (15.8) ~U (18.9)	0.346	[0.39 π]
ADV (11.2) ~U (21.8)	–0.001	[0.50 π]	ADV (10.4) ~U (18.9)	0.065	[0.48 π]
WAV (8.6) ~U (21.8)	–0.611	[0.71 π]	WAV (4.6) ~U (18.9)	–0.984	[0.94 π]
SUM (5.3) ~U (21.8)	0.050	[0.48 π]	SUM (4.6) ~U (18.9)	0.057	[0.48 π]
ADV (11.2) ~GWD (10.4)	–0.887	[0.85 π]	ADV (10.4) ~GWD (15.8)	–0.914	[0.87 π]
WAV (8.6) ~GWD (10.4)	0.420	[0.36 π]	WAV (4.6) ~GWD (15.8)	–0.506	[0.67 π]
SUM (5.3) ~GWD (10.4)	0.909	[0.14 π]	SUM (4.6) ~GWD (15.8)	0.957	[0.09 π]
WAV (8.6) ~ADV (11.2)	–0.791	[0.79 π]	WAV (4.6) ~ADV (10.4)	0.113	[0.46 π]
SUM (5.3) ~ADV (11.2)	–0.999	[0.98 π]	SUM (4.6) ~ADV (10.4)	–0.992	[0.96 π]
SUM (5.3) ~WAV (8.6)	0.760	[0.23 π]	SUM (4.6) ~WAV (4.6)	–0.233	[0.57 π]

SUM tendency, but the latter (Fig. 4(g)) peaks a phase lead of almost $\pi/2$ before the SUM tendency (Fig. 4(i)). This phase shift between Fig. 4(b) and (g) results from the meridional structure of the WAV (not shown). For the average between 2°S and 2°N, the WAV forcing makes a positive contribution to the SUM tendency, but for the average between 10°S and 10°N it makes no contribution to the SUM but decelerates the zonal wind. As a result, the WAV forcing drives the descent of the QBO phase together with the GWD forcing over the equator and spreads out the easterly or westerly momentum poleward to the extratropics.

The ADV tendency (Fig. 4(c, h)) peaks at a phase lead of near π before the SUM tendency. The ADV tendency averaged between 2°S and 2°N (Fig. 4(c)) is a little larger than that averaged between 10°S and 10°N (Fig. 4(h)) because both the vertical motion and the shear ($\omega \frac{\partial u}{\partial p}$) are larger at the equator. The ADV forcing makes a negative contribution to the SUM tendency, cancelling out much of the combined positive contribution from the GWD and WAV and hindering the downward propagation of the QBO phase. The vertical advection dominates in the ADV forcing (more than 80%; not shown), which is associated with the tropical upwelling from the Brewer–Dobson circulation as documented by Match and Fueglistaler (2020).

A more quantitative description of the forcing contribution to the simulated QBO at 5 hPa and phase relations is given by using the projection of the forcing components onto the SUM in Table 1. Since the Pearson linear correlation coefficient is the cosine of the phase difference, the projection is simply the amplitude of the forcing multiplied by the correlation coefficient. At the equator, GWD ($10.4 \times 0.909 = 9.5 \text{ m s}^{-1}/\text{month}$) and WAV ($8.6 \times 0.760 = 6.5 \text{ m s}^{-1}/\text{month}$) are the leading contributions ($6.5 + 9.5 = 16.0 \text{ m s}^{-1}/\text{month}$) to drive the QBO, forcing the descent of the zonal wind shear, while ADV offsets these contributions ($11.2 \times (-0.999) = -11.2 \text{ m s}^{-1}/\text{month}$) with a remainder of $4.8 \text{ m s}^{-1}/\text{month}$, which is close to $5.3 \text{ m s}^{-1}/\text{month}$ shown in Table 1. However, in the tropics between 10°S and 10°N, GWD becomes the sole leading contribution ($15.8 \times 0.957 = 15.1 \text{ m s}^{-1}/\text{month}$) to drive the QBO, while ADV offsets this contribution ($10.4 \times (-0.992) = -10.3 \text{ m s}^{-1}/\text{month}$) with a remainder of $4.8 \text{ m s}^{-1}/\text{month}$, which is close to $4.6 \text{ m s}^{-1}/\text{month}$ shown in Table 1. As a result, the phase shift between ADV and SUM is mainly due to the upwelling in the Brewer–Dobson circulation; the phase shift between GWD and SUM is relatively small, which is caused by the leading contribution of convectively generated GWs; the phase shift between WAV and SUM is between ~ 0 and $\pi/2$, which is mainly linked with the larger convergence of meridional zonal momentum flux by the resolved-scale transient waves in the late half of the easterly and westerly phase than in their early half.

As a qualitative reference, we have made comparisons with the reanalysis results (including ERAI, NCEP-2, and MERRA-2; not shown). Although there are relatively large uncertainties in the forcing terms, in

particular the forcing term of the resolved-scale wave (WAV), the basic features of the QBO forcing terms are qualitatively consistent with the model's simulation as follows: (1) GWD forcing is about 1.1–2.5 times that of SUM in an almost synchronized manner; (2) ADV forcing offsets about 30%–60% of GWD forcing; (3) WAV forcing may have a positive contribution to SUM with a phase shift of $0-\pi/2$, with relatively large uncertainties in both phase difference and magnitude.

4. Summary and discussion

The QBO is reasonably simulated in IAPL69, showing downward propagation of easterlies and westerlies with comparable period and meridional structure relative to ERAI reanalysis. The amplitude is larger than observation ($\sim 33 \text{ m s}^{-1}$ vs. $\sim 28 \text{ m s}^{-1}$ in zonal wind) owing largely to the stronger westerly in the model. Also, the maximum of the simulated QBO zonal wind is higher than in ERAI, as seen in many GCMs (Schenzinger et al., 2017).

The zonal wind time tendency of the QBO is diagnosed by showing four leading terms: convectively generated gravity wave drag (GWD), advection tendency (ADV) by the zonally averaged meridional circulation, resolved-scale waves (WAV), and residual tendency (RES). We have found that, in the formation of the simulated QBO, GWD, and ADV dominate the zonal wind tendency. GWD contributes directly to the zonal wind tendency and forces the downward propagation of the zonal wind shear. ADV cancels out most of the contribution of GWD forcing via the equatorial upwelling of the Brewer–Dobson circulation in the stratosphere. WAV presents as a positive contribution to the zonal wind tendency of the QBO over the equator together with GWD.

In terms of the phase relationships between the processes, relative to the total tendency SUM, the waveform of GWD lags by a phase of less than $\pi/4$. The waveform of WAV leads by a phase of less than $\pi/4$ to SUM. The combination of these two processes makes SUM lead by a phase of $\pi/2$ to the zonal wind, which steers the evolution of zonal wind with time. This combination is offset more than half by ADV.

The above analyses suggest that multiple processes are at play in the evolution of the QBO. Differences in any of the leading processes discussed above can result in different features of the simulated QBO or the disappearance of the QBO in the case of sufficiently strong equatorial upwelling, consistent with the previous work of Dunkerton (1991). Simulation of a more realistic QBO in models likely requires good simulation in all these processes. It would be interesting to examine how the momentum budget in different models compares. A follow-up study will discuss the sensitivities of the forcing processes to different model resolutions and other configurations along with the accompanying QBO.

Funding

This research was supported by the National Major Research High Performance Computing Program of China [grant number 2016YFB0200800], the National Natural Science Foundation of China [grant numbers 41630530 and 41706036], and the National Key Scientific and Technological Infrastructure project “Earth System Science Numerical Simulator Facility” (EarthLab).

Acknowledgments

We gratefully acknowledge the assistance of Dongling Zhang in supporting computing resources to facilitate the development of IAP-AGCM. We also thank Jiangbo Jin for providing useful experimental design advice for evaluating the simulations in IAP-AGCM.

Supplementary materials

Supplementary material associated with this article can be found, in the online version, at [doi:10.1016/j.aosl.2020.100021](https://doi.org/10.1016/j.aosl.2020.100021).

References

- Baldwin, M.P., Gray, L.J., Dunkerton, T.J., Hamilton, K., Haynes, P.H., Randel, W.J., Holton, J.R., et al., 2001. The quasi-biennial oscillation. *Rev. Geophys.* 39 (2), 179–229. doi:10.1029/1999RG000073.
- Beres, J.H., Alexander, M.J., Holton, J.R., 2004. A method of specifying the gravity wave spectrum above convection based on latent heating properties and background wind. *J. Atmos. Sci.* 61 (3), 324–337. doi:10.1175/1520-0469(2004)061<0324:AMOSTG>2.0.CO;2.
- Beres, J.H., Garcia, R.R., Boville, B.A., Sassi, F., 2005. Implementation of a gravity wave source spectrum parameterization dependent on the properties of convection in the Whole Atmosphere Community Climate Model (WACCM). *J. Geophys. Res.: Atmos.* 110 (D10). doi:10.1029/2004JD005504.
- Butchart, N., Anstey, J.A., Hamilton, K., Osprey, S., McLandress, C., Bushell, A.C., Kawatani, Y., et al., 2018. Overview of experiment design and comparison of models participating in phase 1 of the SPARC Quasi-Biennial Oscillation initiative (QBOi). *Geosci. Model Dev.* 11 (3), 1009–1032. doi:10.5194/gmd-11-1009-2018.
- Chai, Z.Y., Zhang, M.H., Zeng, Q.C., Zhang, H., Jin, J.B., Xie, J.B., You, T., 2020. A high-top version of the IAP-AGCM: preliminary assessment and sensitivity. *Atmos. Ocean. Sci. Lett.* In Press.
- Coy, L., Wargan, K., Molod, A.M., McCarty, W.R., Pawson, S., 2016. Structure and dynamics of the quasi-biennial oscillation in MERRA-2. *J. Clim.* 29 (14), 5339–5354. doi:10.1175/JCLI-D-15-0809.1.
- Dee, D.P., Uppala, S.M., Simmons, A.J., Berrisford, P., Poli, P., Kobayashi, S., Andrae, U., et al., 2011. The ERA-Interim reanalysis: configuration and performance of the data assimilation system. *Q. J. R. Meteorol. Soc.* 137 (656), 553–597. doi:10.1002/qj.828.
- Dunkerton, T.J., 1991. Nonlinear propagation of zonal winds in an atmosphere with Newtonian cooling and equatorial wave driving. *J. Atmos. Sci.* 48 (2), 236–263. doi:10.1175/1520-0469(1991)048<0236:NPOZWI>2.0.CO;2.
- Garcia, R.R., Richter, J.H., 2019. On the momentum budget of the quasi-biennial oscillation in the whole atmosphere community climate model. *J. Atmos. Sci.* 76 (1), 69–87. doi:10.1175/JAS-D-18-0088.1.
- Geller, M.A., Zhou, T.H., Shindell, D., Ruedy, R., Aleinov, I., Nazarenko, L., Tausnev, N.L., et al., 2016. Modeling the QBO-improvements resulting from higher-model vertical resolution. *J. Adv. Model. Earth Syst.* 8 (3), 1092–1105. doi:10.1002/2016MS000699.
- Giorgetta, M.A., Manzini, E., Roeckner, E., Esch, M., Bengtsson, L., 2006. Climatology and forcing of the quasi-biennial oscillation in the MAECHAM5 model. *J. Clim.* 19 (16), 3882–3901. doi:10.1175/JCLI3830.1.
- Holton, J.R., Lindzen, R.S., 1972. An updated theory for the quasi-biennial cycle of the tropical stratosphere. *J. Atmos. Sci.* 29 (6), 1076–1080. doi:10.1175/1520-0469(1972)029<1076:AUTFTQ>2.0.CO;2.
- Holton, J.R., Tan, H.C., 1980. The influence of the equatorial quasi-biennial oscillation on the global circulation at 50 mb. *J. Atmos. Sci.* 37 (10), 2200–2208. doi:10.1175/1520-0469(1980)037<2200:TQTEQ>2.0.CO;2.
- Kim, H., Son, S.W., Yoo, C., 2020. QBO modulation of the MJO-related precipitation in East Asia. *J. Geophys. Res.: Atmos.* 125 (4). doi:10.1029/2019JD031929.
- Lindzen, R.S., 1987. On the development of the theory of the QBO. *Bull. Am. Meteorol. Soc.* 68 (4), 329–337. doi:10.1175/1520-0477(1987)068<0329:OTDOTT>2.0.CO;2.
- Lindzen, R.S., Holton, J.R., 1968. A theory for the quasi-biennial oscillation. *J. Atmos. Sci.* 25 (6), 1095–1107. doi:10.1175/1520-0469(1968)025<1095:ATOTQB>2.0.CO;2.
- Lott, F., Denvil, S., Butchart, N., Cagnazzo, C., Giorgetta, M.A., Hardiman, S.C., Manzini, E., et al., 2014. Kelvin and Rossby-gravity wave packets in the lower stratosphere of some high-top CMIP5 models. *J. Geophys. Res.: Atmos.* 119 (5), 2156–2173. doi:10.1002/2013JD020797.
- Match, A., Fueglistaler, S., 2020. Mean flow damping forms the buffer zone of the quasi-biennial oscillation: 1d theory. *J. Atmos. Sci.* (6) 77. doi:10.1175/JAS-D-19-0293.1.
- McFarlane, N.A., 1987. The effect of orographically excited gravity wave drag on the general circulation of the lower stratosphere and troposphere. *J. Atmos. Sci.* 44 (14), 1775–1800. doi:10.1175/1520-0469(1987)044<1775:TEOEG>2.0.CO;2.
- Naujokat, B., 1986. An update of the observed quasi-biennial oscillation of the stratospheric winds over the tropics. *J. Atmos. Sci.* 43 (17), 1873–1877. doi:10.1175/1520-0469(1986)043<1873:AUOTOQ>2.0.CO;2.
- Neale, R.B., Gettelman, A., Park, S., Conley, A.J., Kinnison, D., Marsh, D., Smith, A.K., et al., 2012. Description of the NCAR Community Atmosphere Model (CAM5.0). NCAR Technical Note. National Center for Atmospheric Research.
- Pawson, S., Fiorino, M., 1998. A comparison of reanalyses in the tropical stratosphere. Part 2: the quasi-biennial oscillation. *Clim. Dyn.* 14 (9), 645–658. doi:10.1007/s003820050247.
- Randel, W.J., Wu, F., 1996. Isolation of the ozone QBO in SAGE II data by singular-value decomposition. *J. Atmos. Sci.* 53 (17), 2546–2559. doi:10.1175/1520-0469(1996)053<2546:IOTOQI>2.0.CO;2.
- Ricciardulli, L., Garcia, R.R., 2000. The excitation of equatorial waves by deep convection in the NCAR Community Climate Model (CCM3). *J. Atmos. Sci.* 57 (21), 3461–3487. doi:10.1175/1520-0469(2000)057<2.0.CO;2.
- Richter, J.H., Sassi, F., Garcia, R.R., 2010. Toward a physically based gravity wave source parameterization in a general circulation model. *J. Atmos. Sci.* 67 (1), 136–156. doi:10.1175/2009JAS3112.1.
- Richter, J.H., Solomon, A., Bacmeister, J.T., 2014. On the simulation of the quasi-biennial oscillation in the community atmosphere model, version 5. *J. Geophys. Res.: Atmos.* 119 (6), 3045–3062. doi:10.1002/2013JD021122.
- Scaife, A.A., Butchart, N., Warner, C.D., Stainforth, D., Norton, W., Austin, J., 2000. Realistic quasi-biennial oscillations in a simulation of the global climate. *Geophys. Res. Lett.* 27 (21), 3481–3484. doi:10.1029/2000GL011625.
- Schenzinger, V., Osprey, S., Gray, L., Butchart, N., 2017. Defining metrics of the quasi-biennial oscillation in global climate models. *Geosci. Model Dev.* 10 (6), 2157–2168. doi:10.5194/gmd-10-2157-2017.
- Sun, H.C., Zhou, G.Q., Zeng, Q.C., 2012. Assessments of the climate system model (CAS-ES-M-C) using IAP AGCM4 as its atmospheric component. *Chin. J. Atmos. Sci.* 36 (2), 215–233.
- Taylor, K.E., Stouffer, R.J., Meehl, G.A., 2012. An overview of CMIP5 and the experiment design. *Bull. Am. Meteorol. Soc.* 93 (4), 485–498. doi:10.1175/BAMS-D-11-00094.1.
- Wang, J.B., Kim, H.M., Chang, E.K.M., 2018. Interannual modulation of Northern Hemisphere winter storm tracks by the QBO. *Geophys. Res. Lett.* 45 (6), 2786–2794. doi:10.1002/2017GL076929.
- Yu, C., Xue, X.H., Wu, J.F., Chen, T.D., Li, H.M., 2017. Sensitivity of the quasi-biennial oscillation simulated in WACCM to the phase speed spectrum and the settings in an inertial gravity wave parameterization. *J. Adv. Model. Earth Syst.* 9 (1), 389–403. doi:10.1002/2016MS000824.
- Zhang, G.J., McFarlane, N.A., 1995. Sensitivity of climate simulations to the parameterization of cumulus convection in the Canadian Climate Centre general circulation model. *Atmos. Ocean* 33 (3), 407–446. doi:10.1080/07055900.1995.9649539.
- Zhang, H., 2009. Development of IAP Atmospheric General Circulation Model Version 4.0 and its Climate Simulations. PhD. Diss. (In Chinese).
- Zhang, H., Zhang, M., Jin, J., Fei, K., Ji, D., Wu, C., Zhu, J., et al., 2020. CAS-ESM 2: description and climate simulation performance of the Chinese Academy of Sciences (CAS) earth system model (ESM) version 2. *J. Adv. Model. Earth Syst.* doi:10.1029/2020MS002210.
- Zhang M., H., Zhang, M.H., Zeng, Q.C., 2013. Sensitivity of simulated climate to two atmospheric models: interpretation of differences between dry models and moist models. *Mon. Weather Rev.* 141 (5), 1558–1576. doi:10.1175/MWR-D-11-00367.1.